



# Mechanical properties and deformation morphologies of covalently bridged multi-walled carbon nanotubes: Multiscale modeling

Xu Huang, Hongyan Yuan, Wentao Liang, Sulin Zhang\*

Department of Engineering Science and Mechanics, The Pennsylvania State University, University Park, PA 16802, USA

## ARTICLE INFO

### Article history:

Received 18 March 2010

Received in revised form

25 May 2010

Accepted 7 August 2010

### Keywords:

Multi-walled carbon nanotubes

Quasi-continuum method

Covalent bridge

Buckling

Shape transition

## ABSTRACT

We formulate a multiscale modeling framework to investigate the deformation morphologies and energetics of covalently bridged multi-walled carbon nanotubes (MWCNTs). The formulation involves extending a previously established quasi-continuum model by incorporating the inter-wall bridging energy density function into the constitutive relations via message passing from fully atomistic simulations. Using the extended numerical model, we studied the mechanical responses of the 10-walled MWCNT with varying inter-wall bridge densities under torsion, bending, and uniaxial compression. Our simulation results show that the presence of inter-wall covalent bridges not only enhances the post-buckling rigidities of the MWCNTs, but also modifies the deformation morphologies and morphology pathways. For bending and uniaxial compression, we constructed in the space of bridge density and applied strain the deformation morphology phase diagram, where three phases, uniformly deformed phase, rippling pattern, and diamond-shaped pattern, are identified and separated by linear phase boundaries. We attribute the deformation phase transitions to the interplay of inter-wall and intra-wall interaction energies. The multiple shape transitions of MWCNTs and the elastic nature of the deformation suggest that MWCNTs can be designed as shape-memory nanodevices with tunable stabilities.

© 2010 Elsevier Ltd. All rights reserved.

## 1. Introduction

Owing to its large in-plane rigidity as compared to its bending rigidity (Lee et al., 2008), graphene shell often deforms nearly isometrically, featuring local sharp folds. Such deformation morphologies have been widely observed in previous studies: edge-induced warping in free-standing monolayer graphene (Shenoy et al., 2008); local kinks in bent single-walled carbon nanotubes (SWCNTs) (Fig. 1(a) and (b)) (Yakobson et al., 1996); belt-like structures in strongly twisted SWCNTs (Fig. 1(c)) (Yakobson et al., 1996). These load-driven morphologies not only indicate the stability of the graphene shells, but also alter their electronic properties (Tomblor et al., 2000; Yang and Han, 2000) due to the intrinsic coupling between mechanical and electrical responses. The deformation morphologies are generally reversible upon unloading (Iijima et al., 1995; Falvo et al., 1997), suggesting the high deformability and the pure elastic nature of graphene shells.

While the instability of deformed SWCNTs follows the classical beam or shell theories (Yakobson et al., 1996; Zhang et al., 2005), the physical mechanism of the deformation patterns observed in deformed thick multi-walled carbon nanotubes (MWCNTs) appears to be more complex. MWCNTs are composed of concentric graphene shells with extremely

\* Corresponding author. Tel: +1 814 865 7640; fax: +1 814 865 9974.

E-mail address: [suz10@psu.edu](mailto:suz10@psu.edu) (S. Zhang).

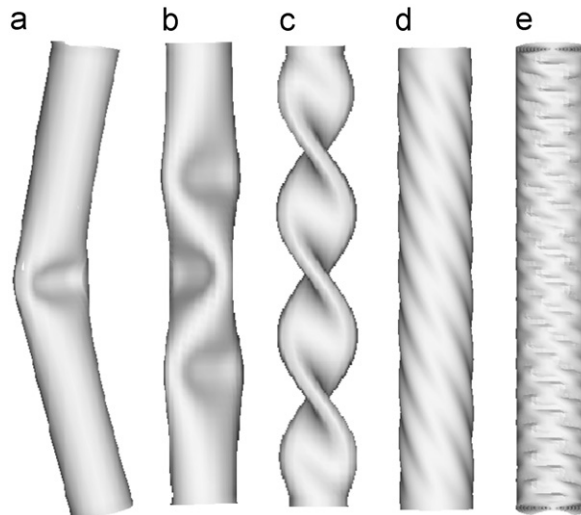


**Fig. 1.** Representative buckling morphologies of SWCNTs and MWCNTs: (a) a local kink in a bent (10,10) SWCNT; (b) buckling mode in a compressed (10,10) SWCNT; (c) belt-like structure of a twisted (10,10) SWCNT; (d) rippled 10-walled MWCNT; and (e) diamond-shaped pattern in a 10-walled bent MWCNT.

strong covalent bonding interactions within each shell but weak inter-wall van der Waals (vdW) interactions. The weak inter-wall interactions may be exploited in a variety of applications, where MWCNTs are used as low friction components of nanomechanical devices such as nanoscale motors (Fennimore et al., 2003), bearings (Kolmogorov and Crespi, 2000; Zhang et al., 2004a), oscillators (Zheng and Jiang, 2002; Legoas et al., 2003; Zou et al., 2006), nanosensors (Gao et al., 2003; Zou et al., in press), etc. On the other hand, the ultra-low inter-wall shear resistance indicates very low load transfer between the shells (Kis et al., 2004), presenting a major concern for using MWCNT and CNT bundles as mechanical reinforcements in polymeric composites (Qian et al., 2000). However, owing to the spatial confinement of the constituent shells, radial deformation of constituent shells relative to each other causes significant inter-wall interaction energy penalty, which suggests that MWCNTs may adopt different deformation mechanisms from that of an isolated graphene shell. Recent studies (Arias and Arroyo, 2008; Huang et al., 2008b) showed that the wave-like rippling pattern (Fig. 1(d)) in twisted MWCNTs is far away from isometric deformation. In contrast, the Yoshimura pattern (diamond-shaped pattern, Fig. 1(e)) is fairly close to be isometric. The different deformation morphologies indicate that the inter-wall interaction energies play a critical role in determining the deformation shape space of MWCNTs, which remains less understood from previous studies.

When covalent bridges are introduced between neighboring graphene shells in an MWCNT or CNT bundle, the inter-wall interaction is amplified, which subsequently influences the energetics of MWCNT deformation. Recent experiments demonstrated that inter-wall covalent bonds introduced through electron-beam irradiations may significantly enhance the inter-wall shear resistance of SWCNT bundles (Kis et al., 2004). If a spot is repeatedly impacted, large open ring defects may be created, which would initiate fracture upon tensile loading (Zhang et al., 2005, 2007b). Under moderate electron energies and relatively low doses, the most prolific defect produced is the single-atom defects (Krasheninnikov et al., 2002; Zhang et al., 2004b; Terdalkar et al., 2008), i.e., single-atom vacancies, inter-wall interstitials, and Frankel defects (interstitial–vacancy pairs). Due to their relatively low migration barriers ( $\sim 1$  eV) (Krasheninnikov et al., 2006), these single-atom defects are highly mobile even at moderate temperatures. An interstitial falling in between two neighboring graphene shells in an MWCNT or in CNT bundles becomes four-coordinated by interacting with the nearest four atoms from the neighboring shells, forming an inter-wall  $sp^3$  bridge (Fig. 2(a)). Unlike metals where a single-atom vacancy is essentially a missing atom in the lattice, a single-atom vacancy in  $sp^2$  hexagonal network is subjected to bond reconstruction, where two of the three dangling bonds associated with the missing atom join to form a new bond. The bond reconstruction yields an energetically more stable configuration. When two such reconstructed single-atom vacancies from neighboring shells are in proximity, an inter-wall covalent bond may be created by saturating the third dangling bond of each vacancy (Telling et al., 2003; Kis et al., 2004), forming an inter-wall divacancy (see Fig. 2(b) and (c)). Depending on the orientation of the divacancy relative to the axial direction of the tube, two types of such divacancies can be produced. One type involves two single-atom vacancies that are oriented perpendicularly (Fig. 2(b)), while the other involves two single-atom vacancies that are oriented in parallel (Fig. 2(c)). Once a covalent bridge is formed, the migration barrier of the associated single-atom defects increases markedly, which effectively immobilizes the defects at room temperature.

In this article, we extend the existing quasi-continuum method (Arroyo and Belytschko, 2002) by incorporating the effects of inter-wall covalent bridges. With the extended quasi-continuum method, we systematically investigate the deformation morphologies and energetics of covalently bridged MWCNTs. Our simulation results show that the inter-wall

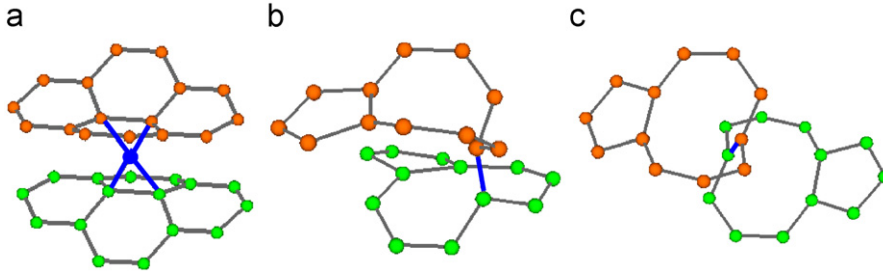


**Fig. 2.** Three types of inter-wall bridges between graphene shells. Atoms colored differently (red and green) belong to different walls: (a) an  $sp^3$  bridge formed by an interstitial (colored by blue); (b) an  $sp^2$  bridge formed by two single-atom vacancies oriented perpendicularly; and (c) an  $sp^2$  bridge formed by two single-atom vacancies oriented in parallel. (For interpretation of the references to color in this figure legend, the reader is referred to the web version of this article.)

covalent bridges not only enhance the mechanical properties of the MWCNTs, but also influence their deformation morphologies. In Section 2, we will introduce the extended quasi-continuum model, where the inter-wall interaction energy is homogenized through message passing from atomistic simulations. In Section 3, we will present the mechanical properties and the deformation morphologies of the MWCNTs. Energetic analyses are performed in Section 4 to elucidate the deformation phase transition mechanisms. Discussions and conclusions are provided in Section 5.

## 2. Extended quasi-continuum model

All-atom molecular dynamics/mechanics (MD/MM) simulations with empirical force fields have been routinely performed to study the inter-wall bridge formation due to ion irradiations and the mechanical properties of bridged MWCNTs and CNT bundles (Xia et al., 2007; Song and Zha, 2009). However, these studies have been limited to SWCNTs or MWCNTs with only a few graphene shells due to the large computational cost. To span the accessible length scales, a number of coarse-grained approaches have been proposed (Arroyo and Belytschko, 2002; Zhang et al., 2002; Pantano et al., 2003; Buehler, 2006; Cao and Chen, 2006; Zhang et al., 2007a; Zou et al., 2009). Since the deformed shells exhibit material and geometry nonlinearities, models with correct infinitesimal moduli describe only qualitatively the large deformation mechanics of MWCNTs. In our simulations, we extend the quasi-continuum model of Arroyo and Belytschko (2002) for graphene shells by including the effects of inter-wall covalent bridges. In this model, the elasticity of the monolayer graphene shell is systematically inherited from the underlying interatomic potentials. Therefore, material nonlinearity is faithfully incorporated. The discrete sum of inter-wall vdW interactions is replaced by integrals over graphene surfaces through homogenization, thereby substantially improving computational efficiency. The in-plane and out-of-plane elasticity furnishes the constitutive law governing the mechanical responses of the MWCNTs, and can be conveniently implemented in a standard finite element framework. As extensively tested (Arroyo and Belytschko, 2002, 2003, 2004; Arias and Arroyo, 2008; Arroyo and Arias, 2008; Huang et al., 2008b, 2010), the coarse-grained model accurately reproduces atomistic simulations and the computational efficiency is improved by about two orders of magnitude as compared to its atomistic counterpart. A comprehensive description of this quasi-continuum model can be found in relevant references (Arroyo and Belytschko, 2002, 2004). For completeness, the essential idea of the quasi-continuum model is also revisited in our following discussions.

### 2.1. Interaction potentials

We adopt the modified second-generation Tersoff–Brenner potential (Shenderova et al., 2000; Belytschko et al., 2002; Brenner et al., 2002), denoted by MTB-G2, to describe the bonded C–C interactions, as

$$E = \sum_i \sum_j V^R(r_{ij}) - b_{ij} V^A(r_{ij}) \quad (1)$$

where  $r_{ij}$  is the distance between atoms  $i$  and  $j$ ,  $V^R$  and  $V^A$  are the pair-wise repulsive and attractive interaction potentials, respectively,  $b_{ij}$  is the bond-order function that has a complicated dependence on the bond angles and bond lengths involving atoms  $i$  and  $j$ .

The inter-wall vdW interaction is described by the classical Lennard–Jones (LJ) potential (Girifalco et al., 2000) as

$$V_{\text{nb}}(r) = \frac{\eta}{r_0^6} \left[ \frac{1}{2} \lambda^6 \left( \frac{r_0}{r} \right)^{12} - \left( \frac{r_0}{r} \right)^6 \right] \quad (2)$$

where  $r$  is the interatomic distance,  $\lambda=2.7$  is a dimensionless constant,  $r_0=1.42 \text{ \AA}$  is the equilibrium bond length, and  $\eta=1.52 \text{ eV \AA}^6$ . When self-adhesion of an individual shell is not a concern, vdW interactions for carbon atoms on the same shell are neglected and only inter-wall vdW interactions are taken into account.

## 2.2. Force-separation law of inter-wall bridges

To establish the force-separation law of the inter-wall bridges, we set up a simulation model consisting of a (5,5)/(10,10) double-walled CNT (DWCNT) of  $\sim 60$  Å in length. A single inter-wall covalent bridge, shown in Fig. 3, is introduced to bridge the walls. For the two types of  $sp^2$  bridges, only the type shown in Fig. 2(c) is considered in our simulations; results for the other type are quantitatively similar. In our simulations, vdW interactions are not included. The covalently bridged DWCNT is fully relaxed free of any constraints using a limited memory BFGS geometry optimization algorithm (Liu and Nocedal, 1989). The relaxed configuration is adopted as an initial geometry for determining the shearing and normal pulling responses of the DWCNT. To obtain the normal pulling response, roughly half side of each wall cut from the radial direction is held fixed. The fixed sides are the lower sides of inner tubes and the upper sides of outer tubes in Fig. 3(a) and (b). Incrementally moving the inner fixed side downward and the outer fixed side upward effectively pulls the two walls apart. To realize the shear displacement, one end of each tube is fixed by constraining a ring of carbon atoms, while the other end is completely free. The fixed ends of these two tubes are opposite to each other with one on the left side while the other on the right. The two tubes are sheared by incrementally moving the fixed rings of atoms in the opposite directions until the bridge breaks. For either loading case, the DWCNT is relaxed at each incremental loading step, and the total system potential energy is calculated. As a critical normal or shear displacement, the pulling/shearing force abruptly drops, indicating the breakage of the inter-wall bridge.

The potential energy of inter-wall bridges, denoted by  $V_{bg}$ , is composed of two parts, which in general can be written as

$$V_{bg} = V_r + V_\theta, \quad (3)$$

where  $V_r$  and  $V_\theta$  are, respectively, due to the change of the length and angle of the bridge. Normal pulling only stretches the bond, which gives rise to the potential energy function  $V_r$ . Shearing of the two tubes changes both the length and the angle of the bridges. Combining the simulations of the two loading conditions, the potential energy function  $V_\theta$  can be obtained. To simplify our analysis, the potential energies are approximated by quadratic functions,

$$V_r = \frac{1}{2}k_r(r-r_0)^2 \quad (4a)$$

$$V_\theta = \frac{1}{2}k_\theta(\theta-\theta_0)^2 \quad (4b)$$

where  $k_r$  and  $k_\theta$  are the stiffnesses. The parameters of the quadratic functions obtained from our simulations are listed in Table 1.

Due to the presence of the inter-wall bridges, the two-tube bundles or MWCNTs are pre-strained. The bond lengths  $r_0$  are chosen such that the reference state of the continuum model, as presented below, builds up the same amount of pre-strain energy as the atomistic model. This criterion coincidentally leads to  $r_0 \approx 0.28$  nm for both bridge types. The bond angle for the  $sp^3$  bridges is zero with respect to the radial direction. However, for the  $sp^2$  bridges in the fully relaxed state the bond angle is non-zero with respect to the radial direction. In our simulations, we also set  $\theta_0$  for the  $sp^2$  bridges to be zero to reflect the statistics of the  $sp^2$  bridge angles (can be positive and negative). Further, there exists a critical bridge length beyond which the bridge breaks. We note that the bridge angle negligibly affects the critical bridge length. Thus, the cutoff lengths of the two types of bridges are set to be those obtained from normal pulling simulations.

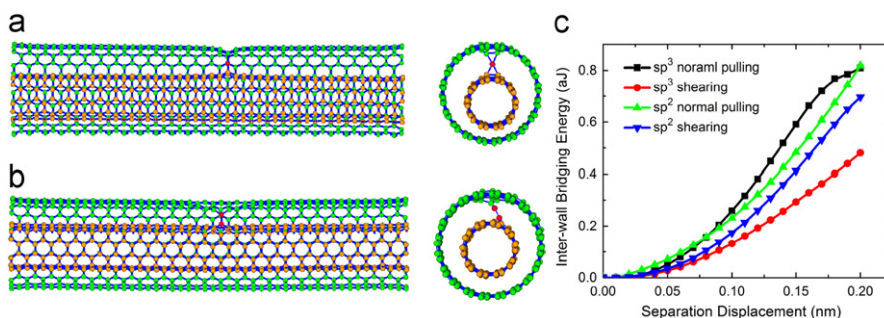


**Fig. 3.** All-atom molecular mechanics simulations of the mechanical responses of the inter-wall bridges. (a) A (5,5)/(10,10) DWCNT tube bridged by an  $sp^3$  bond. Left: side view; right: cross-sectional view. (b) A (5,5)/(10,10) DWCNT tube bridged by an  $sp^2$  bond (shown in Fig. 2(c)). Left: side view; right: cross-sectional view. (c) Potential energies of the covalent bridges under imposed normal and shear pulling displacements.

**Table 1**

Potential parameters for the inter-wall bridges.

Bridge type	$r_0$ (nm)	$\theta_0$ (rad)	$k_r$ (aj/nm <sup>2</sup> )	$k_\theta$ (aj/rad <sup>2</sup> )	$r_{cut}$ (nm)
$sp^3$	0.28	0	43.31	2.20	0.52
$sp^2$	0.28	0	34.60	2.54	0.57

### 2.3. Atomistically informed constitutive model for bridged shells

For an atomic system, the total system energy is a discrete sum of the interatomic interaction potentials. To develop a constitutive model of the continuum counterpart, these discrete energies need to be homogenized. Homogenization schemes for the three types of interactions, intra-wall covalent binding energy, inter-wall vdW energy, and the inter-wall covalent bridging energy, are described below.

*Intra-wall covalent binding energy:* For space-filling crystalline materials, the standard Cauchy–Born rule (Milstein, 1982) establishes a link between the atomistic and the continuum descriptions for the bonded interactions. The mathematical description of the kinematics coupling is written as

$$\mathbf{a} = \mathbf{F}\mathbf{A} \quad (5)$$

where  $\mathbf{F}$  is the deformation gradient, and  $\mathbf{A}$  and  $\mathbf{a}$  are the lattice vectors in the undeformed and deformed configurations, respectively. However, when mapping the deformation of a single-atom thick crystalline film in a three-dimensional space, the standard Cauchy–Born rule breaks down due to the fact that the lattice vectors in a curved surface are chords and are not tangential to the surface; whereas the deformation gradient  $\mathbf{F}$  operates on vectors tangential to a surface. To overcome this conceptual drawback, an exponential Cauchy–Born rule was proposed (Arroyo and Belytschko, 2002) as

$$\mathbf{a} = \mathcal{F}_\chi \mathbf{A} \quad (6)$$

where  $\mathcal{F}_\chi$  transforms the undeformed lattice vector into a deformed one. Through a local approximation of the exponential map (Arroyo and Belytschko, 2004), the deformed lattice vectors and the angles between two lattice vectors can be analytically represented in terms of the continuum deformation measures of the surface, i.e., the Green deformation tensor  $\mathbf{C}$  and the curvature tensor  $\mathbf{K}$ . We consider a representative unit cell of area  $s_0 = (3\sqrt{3}/2)\|\mathbf{A}_0\|^2$  containing two inequivalent nuclei and three inequivalent bonds in the reference, undeformed configuration. The strain energy of the unit cell  $E_{\text{cell}}$ , and hence the hyperelastic strain energy density  $W$  ( $W(\mathbf{C}; \mathbf{K}) = E_{\text{cell}}/s_0$ ), can be then analytically formulated in terms of underlying interatomic potentials. Thus, the covalent binding energy for the continuum region that is subject to the deformation map  $\phi$  that maps from undeformed to deformed configurations is

$$E_{\text{cv}} = \int_{\Omega_0} W[\mathbf{C}(\phi(\mathbf{X})), \mathbf{K}(\phi(\mathbf{X}))] d\Omega_0 \quad (7)$$

where  $\mathbf{X}$  is a material point in the undeformed configuration of surface area  $\Omega_0$ .

*Inter-wall vdW energy:* Homogenization of the discrete nonbonding energy between two unit cells gives rise to the vdW energy density:

$$\hat{V}_{\text{nb}}(r) = \left(\frac{2}{s_0}\right)^2 V_{\text{nb}}(r) \quad (8)$$

where  $r$  is the separation between two material points. Note that the factor of two on the right-hand side of Eq. (8) comes from the fact that each unit cell contains two nuclei. The continuum form of the nonbonding energy  $E_{\text{nb}}$  is a double integral over two graphene shells:

$$E_{\text{nb}} = \frac{1}{2} \int_{\Omega_{0X}} \int_{\Omega_{0Y}} \hat{V}_{\text{nb}}[|\phi(\mathbf{X}) - \phi(\mathbf{Y})|] d\Omega_{0X} d\Omega_{0Y} \quad (9)$$

where  $\mathbf{X}$  and  $\mathbf{Y}$  are the two material points that sit on two different CNT walls.

*Inter-wall bridging energy:* The inter-wall bridging energy is homogenized in the similar manner as the inter-wall vdW interaction energy. We denote  $\rho = n_{\text{bg}}/s_0$  the inter-wall bridge density, where  $n_{\text{bg}}$  is the number of the covalent bridges in each unit cell. The potential energy density (per unit area) can thus be written as

$$\hat{V}_{\text{bg}} = \rho V_{\text{bg}}(|\phi(\mathbf{X}) - \phi(\mathbf{X}')|) \quad (10)$$

where  $\mathbf{X}$  and  $\mathbf{X}'$  are two material points that are located on neighboring shells, representing the two ends of the inter-wall bridges. The total potential energy due to the inter-wall covalent bridges at the deformed configuration can be written as

$$E_{\text{bg}} = \int_{\Omega_0} \hat{V}_{\text{bg}}(|\phi(\mathbf{X}) - \phi(\mathbf{X}')|) d\Omega_0 \quad (11)$$

Note that the potential energy of the covalent bridges takes a form (single integral) different from that of the vdW interaction energy (double integral). This is due to the fact that, once one end of the intertube covalent bond is identified, the other end is accordingly determined. In our simulations, the wall whose reference configuration contains the material point  $\mathbf{X}$  is treated as the master surface, while the wall whose reference configuration contains the material point  $\mathbf{X}'$  as the slave surface. Unlike the vdW interaction energy where a double integral over both the CNT surfaces is necessary for calculating the total energy contribution, the potential energy due to the covalent bridges involves an integral over only the master surface.

The continuum forms of the three interaction energies furnish the continuum constitutive relations, which facilitate the finite element simulations. In our numerical calculations of the total system energy and the first derivative

(the negative forces), we use 2, 9, and 2 Gauss quadrature points, respectively, to integrate the intra-wall covalent binding energy, the inter-wall vdW energy, and the inter-wall covalent bridging energy.

*The weakening effects of single-vacancy defects:* Previous atomistic and quantum mechanical calculations concluded that the presence of the single-vacancy defect reduces the in-plane stiffness of CNTs (Mielke et al., 2004; Zhang et al., 2005). We have performed systematic studies using a (10,0) tube as a model system, and established a relationship between the reduction percentage  $\alpha$  as a function of the defect density  $\rho$ . The reduction percentage of the in-plane stiffness is nearly proportional to the defect density (Mielke et al., 2007), i.e.,  $\alpha = \eta\rho$ , where  $\eta \approx 3$ , provided that the defects are not sufficiently close to each other such that direct interaction between the defects is non-negligible. Considering that C–C interactions are short-ranged, this assumption is reasonable as long as the defect density is not too high. To account for the weakening effect, we rescale the in-plane covalent binding energy by using  $\eta$  as the scaling factor. Due to this rescaling, the in-plane stiffness is accordingly reduced. Such rescaling has been successfully employed in a previous study (Khare et al., 2007).

*Model validation:* We validate the extended multiscale model by comparing the deformation energetics of a double-walled CNT under compression obtained by the fully atomistic model and by our multiscale model, as shown in Fig. 4. The DWCNT is constituted by a (5,5) inner shell and a (10,10) outer shell, and is 6 nm long. Fully atomistic simulations are performed for the non-bridged DWCNT and the 1%  $sp^3$  bridged DWCNT. While multiscale simulations are performed only for the 1%  $sp^3$  bridged DWCNT. Fig. 4 plots the variation of the deformation energy of the DWCNTs as a function of compression strain. The energy curve of the bridged DWCNT predicted by the multiscale model follows very well with that by the fully atomistic model in the harmonic deformation regime. Both the models predicted that the bridged DWCNT buckles at the strain of  $\sim 5\%$ . Beyond the buckling strain, the energy curve predicted by the multiscale model only slightly deviates from that by the fully atomistic model. Unlike the non-bridged DWCNT for which an abrupt energy drop appears at the buckling point, the transition from the harmonically deformed regime to buckled regime is hardly graphically appreciable, manifesting the strengthening role of the inter-wall bridges, but is distinctly different from that of the non-bridged DWCNT. The deformation energetics of the bridged DWCNT is considerably different from that of the non-bridged one when the compression strength is beyond 4%.

#### 2.4. Pre-buckling properties of MWCNTs

In the pre-buckling regime, an MWCNT can be simply treated as a series of linear springs, where the inter-wall interactions play a negligible role. For an  $n$ -walled MWCNT, the total energy of an MWCNT under torsion, bending, and compression can be written as

$$E_{\text{Total}} = \begin{cases} \pi L \alpha^2 t G_s \sum_{i=1}^n r_i^3 & \text{Twisting} \\ 1/2 \pi L Y_s t \kappa^2 \sum_{i=1}^n r_i^3 & \text{Bending} \\ \pi L Y_s t \varepsilon^2 \sum_{i=1}^n r_i & \text{Compression} \end{cases} \quad (12)$$

where  $\alpha$ ,  $\kappa$ , and  $\varepsilon$  are the torsional angle, bending curvature, and compressive strain, respectively;  $L$  is the length of the MWCNT;  $t$  is the thickness of the graphene wall;  $G_s$  and  $Y_s$  are the shear modulus and Young's modulus of each layer; and  $r_i$  is the radius of the  $i$ th wall in the MWCNT. For the second-generation Brenner potential, analytical models (Chang and Gao, 2003; Arroyo and Belytschko, 2004) predicted the Young's modulus of the shells of  $\sim 243/t$  J/m<sup>2</sup> and the Poisson's ratio of

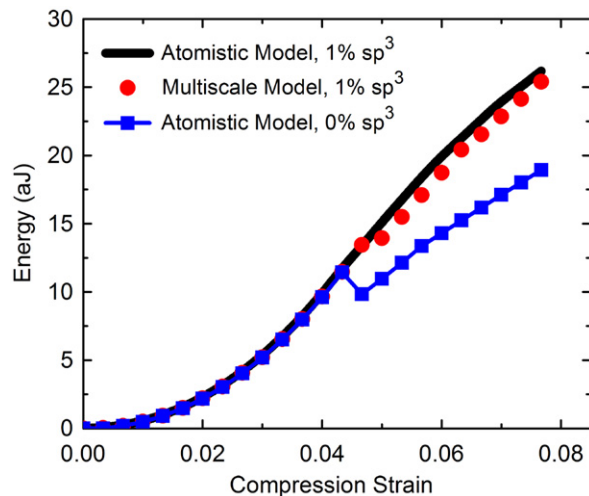


**Fig. 4.** Comparison of the deformation energetics of a double-walled CNT under compression extracted by the fully atomistic model and the multiscale model.

0.397, where  $t=0.066$  nm (Liu et al., 2003). Treating the graphene shell as an isotropic material, one follows  $G_s=86.97/t$  J/m<sup>2</sup>. The torsional, bending, and compression spring constants of the MWCNT are:  $2\pi tG_s \sum_{i=1}^n r_i^3$ ,  $\pi Y_s t \sum_{i=1}^n r_i^3$ , and  $\pi Y_s t \sum_{i=1}^n r_i$ , respectively. For a 10-layer MWCNT, the spring constants are  $6.49 \times 10^4$  nN nm<sup>2</sup>,  $9.36 \times 10^4$  nN nm<sup>2</sup>, and  $2.86 \times 10^4$  nN, respectively. The spring constants will be used to validate our numerical analysis presented below.

### 3. Results and analyses

In this section, we present our simulation results regarding the deformation morphologies and energetics of covalently bridged MWCNTs under bending, twisting, and compression. All the simulations are performed on a 10-walled MWCNT indexed as (5,5)/(10,10)/.../(50,50). Size and chirality effects are of interesting topics but beyond the scope of the present study. The spacing between neighboring shells in the MWCNT is roughly 0.34 nm. The graphene shells in the MWCNT are coarse-grained by finite elements, where the mesh size effect is carefully studied to ensure the simulation convergence. To illustrate the effects of the inter-wall covalent bridges, simulation results of the non-bridged MWCNT are also presented. For a very large inter-wall bridge density, the  $sp^2$ -bridged MWCNT is close to an amorphous diamond. On the other hand, for a very large  $sp^2$  bridge density, interaction between the intra-wall vacancy defects becomes significant. In our simulations, we restrict our simulations to a relatively low bridge density (up to 4%) so that the interstitial carbon atoms do not interact to form extra covalent bonds and the vacancy defects associated with  $sp^2$  bridges do not interact to form large open-ring structures. Since the deformed MWCNTs in our simulations exhibit evolving morphologies, as shown below, we here make a clear distinction between the wave-like rippling pattern and the diamond-shaped (Yoshimura) pattern.

All the simulations presented below are based on ground-state energy minimization, where temperature effects are not taken into account. One notes that at high temperatures, the inter-wall bridges may undergo reconstruction; the single-vacancy defects associated with  $sp^2$  bridges may diffuse along the graphene shells. Thus, our quasi-static simulation results are valid only at relatively low temperatures (up to room temperature).

#### 3.1. Twisting

Deformation morphology and energetics of non-bridged MWCNTs under torsion have been previously studied (Arias and Arroyo, 2008; Huang et al., 2008b; Zou et al., 2009). When the torsional strain (torsional angle per unit length) exceeds a critical value the twisted MWCNTs buckle and exhibit periodic wave-like rippling pattern. The buckling strain scales with  $R^\alpha$ , where  $R$  is the radius of the MWCNT and  $\alpha \approx -1.72$ . The wave number in the circumferential direction varies with the diameter of the MWCNTs. These studies further showed that the torsional response follows a bilinear law, where the ratio of the post-buckling rigidity to the pre-buckling rigidity is nearly constant ( $\sim 0.62$  for the MTB-G2 potential) (Huang et al., 2008b). Here, the post-buckling morphology of the bridged MWCNTs is examined and compared with that of the non-bridged MWCNT.

To study the response of the bridged MWCNTs subject to torsion, the finite element nodes at the ends of the MWCNTs are held fixed. The fixed nodes at one end of the MWCNTs are incrementally rotated with respect to those at the other end, thereby effectively twisting the MWCNTs. The limited-memory BFGS algorithm is implemented to minimize the energy at each loading step, thereby finding stable equilibrium configurations. All the twisted MWCNTs are of 34 nm long. Rippling pattern appears along the MWCNTs when the torsional strain exceeds a critical value. Fig. 5 depicts the longitudinal and cross-sectional views of the rippling morphologies of the  $sp^3$ - and  $sp^2$ -bridged MWCNTs (Fig. 5(a) and (b), respectively) at the applied torsional strain of  $\phi=0.0205$  nm<sup>-1</sup>. In each subfigure, the inter-wall bonding density varies from 0% (non-bridged) to 4% from left to right.

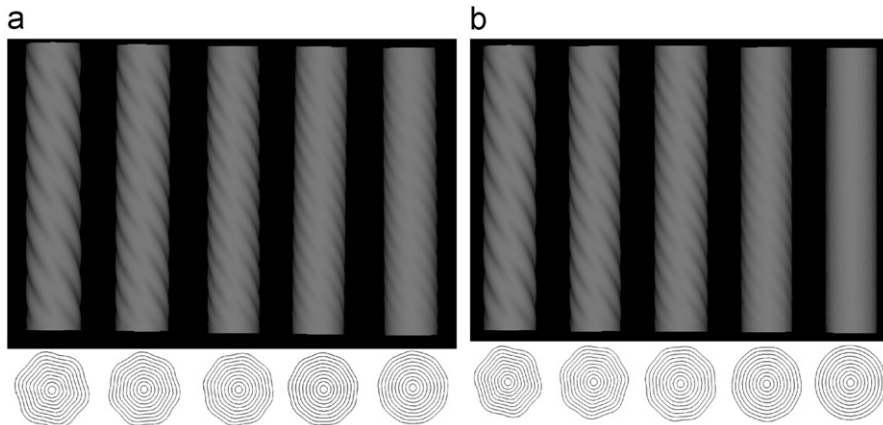


**Fig. 5.** Rippling patterns of twisted MWCNTs at  $\phi=0.0205$  nm<sup>-1</sup> for different inter-wall bridge density  $\rho$ : (a) the  $sp^3$ -bridged MWCNT and (b) the  $sp^2$ -bridged MWCNT. In each subfigure, the inter-wall bridge density ranges from 0% (non-bridged) to 4% from left to right.

(non-bridged) to 4% from left to right. For all the MWCNTs except for that with 4%  $sp^2$  bridges, the cross-sectional views show that the initial circular shape turns into a polygonal shape with rounded corners. For 4%  $sp^2$  inter-wall bridge density, rippling is not graphically distinguishable and the cross-section is deformed into an oval-shaped configuration. Despite that the rippling morphologies are similar, the wave number in the circumferential direction of the rippling patterns monotonically increases with the inter-wall bridge density. For example, for the  $sp^3$ -bridged MWCNTs, the wave number in the circumferential direction changes from 6 to 9 incrementally as the inter-wall bridge density varies from 0% to 4%. The wavelength in the longitudinal direction is inversely proportional to the wave number in the circumferential direction, and thus monotonically decreases with the inter-wall bridge density.

Fig. 6 quantifies rippling amplitudes as a function of the torsional strain (a) ( $\rho=2\%$ ) and inter-wall bridge density (b) in the twisted MWCNTs. Fig. 6(a) shows that at small torsional strains, the MWCNTs uniformly deform without distinguishable rippling. The rippling amplitudes abruptly arise when the torsional strain reaches a critical value, indicating the occurrence of instability due to rippling. The critical torsional strain for the non-bridged MWCNT is much smaller than the bridged ones. Fig. 6(b) shows that with increasing inter-wall bridge density the rippling amplitude decreases monotonically, manifesting the strengthening role of the inter-wall bridges. From an energetics point of view, rippling is driven by the in-plane strain energy release, penalized by the inter-wall interaction energy. Due to the weakening effects of intra-wall defects, the in-plane rigidity of the  $sp^2$ -bridged MWCNT is lower, corresponding to a lower driving force for the rippling pattern. This explains that the rippling amplitudes for the  $sp^3$ -bridged MWCNTs are slightly larger than those of the  $sp^2$ -bridged MWCNTs at small bridge density. For the non-bridged MWCNT, the inter-wall energy penalty for the rippling pattern to occur is the smallest, which explains its highest rippling amplitude.

In Fig. 7 we show the torque–torsional strain relations of the twisted MWCNTs, where the inter-wall bridge density for the bridged MWCNTs is 2%. Each curve exhibits a turning point, corresponding to the rippling strain, which separates the uniformly deformed and rippling regimes. While the rippling strains for the bridged MWCNTs are similar, they are much larger than that of the non-bridged MWCNT. All the curves are approximately bilinear, and the post-rippling rigidities are smaller than the pre-rippling rigidities. Since the inter-wall bridges are inactive in the pre-rippling regime, the pre-rippling rigidities for the  $sp^3$ -bridged and non-bridged MWCNTs are the same, which is slightly larger than that of the

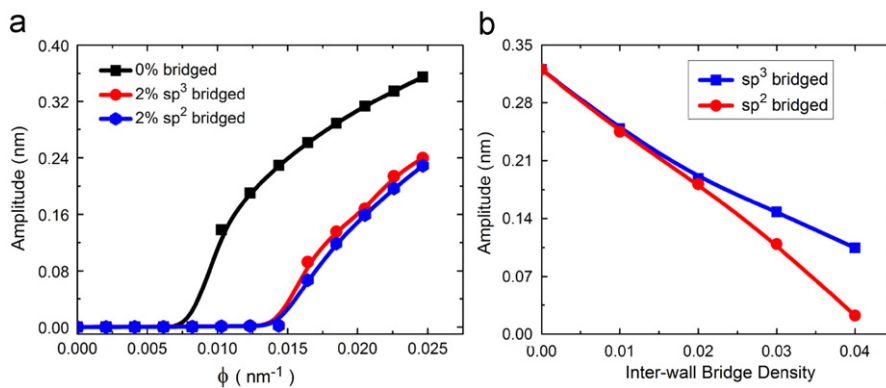


Fig. 6. Rippling amplitude as a function of the torsional strain (a) and of the inter-wall bridge density (b).

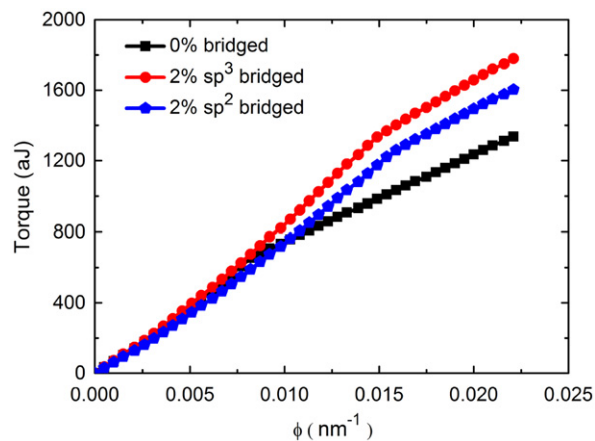
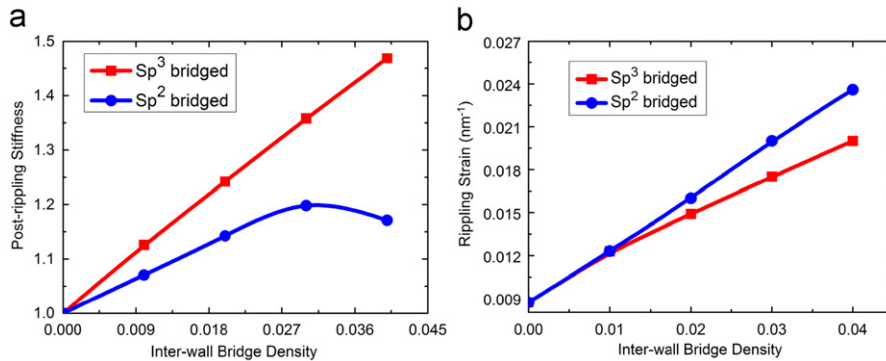


Fig. 7. Torque–torsional strain relation of twisted MWCNTs.



**Fig. 8.** (a) Post-rippling rigidity for the  $sp^3$ -bridged MWCNT increases nearly linearly with inter-wall bridge density. For the  $sp^2$ -bridged MWCNTs, the post-rippling rigidity increases and reaches a peak at  $\rho=3\%$ , beyond which it decreases monotonically due to the weakening effect of intra-wall defects. (b) The rippling strain increases monotonically with inter-wall bridge density.

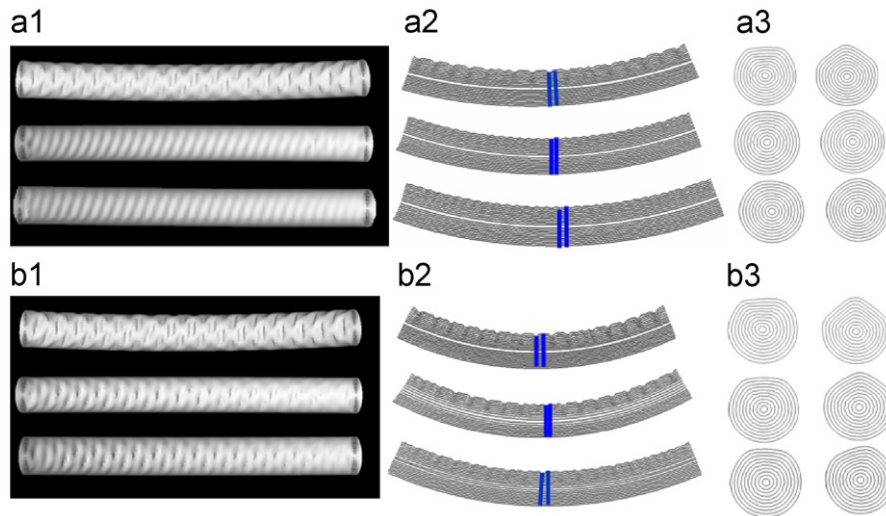
$sp^2$ -bridged MWCNT because of the weakening effect of the intra-wall defects. We note that the pre-rippling rigidity for the  $sp^3$ -bridged and non-bridged MWCNTs is  $6.78 \times 10^4$  nN nm<sup>2</sup>, which is fairly close to the analytical value derived from the Cauchy–Born hypothesis ( $6.49 \times 10^4$  nN nm<sup>2</sup>).

Fig. 8(a) shows the post-rippling rigidities of the bridged MWCNTs, normalized by that of the non-bridged MWCNT, as a function of the inter-wall bridge density. For the  $sp^3$ -bridged MWCNTs, the post-rippling rigidity increases monotonically with the inter-wall bridge density. While for the  $sp^2$ -bridged MWCNTs, the post-rippling rigidity reaches a maximum at  $\rho \sim 3\%$ ; further increasing inter-wall bridge density leads to decreased post-rippling rigidity. This trend can be attributed to the weakening effect of the vacancy defects associated with  $sp^2$  bridges. The post-rippling rigidities of the bridged MWCNTs are much larger than that of the non-bridged one, and comparable to their pre-rippling rigidities. This manifests the strengthening effects of the covalent bridges in MWCNTs. For 4%  $sp^3$ -bridged MWCNT, the post-rippling rigidity increases by 50% as compared to that of the non-bridged MWCNT. Fig. 8(b) shows that the rippling strains for the bridged MWCNTs are fairly close at relatively low inter-wall bridge densities. At a higher inter-wall bridge density, the rippling strains for the  $sp^2$ -bridged MWCNTs are higher than those of the  $sp^3$ -bridged ones, simply because the  $sp^3$ -bridged MWCNTs are more rigid. Due to the strengthening effects of the inter-wall bridges, the rippling strains for the bridged MWCNTs are much larger than that of the non-bridged MWCNT ( $\rho=0$ ).

### 3.2. Bending

A bent SWCNT develops a local kink, much like that seen in a bent drinking straw (Fig. 1(a)). In contrast, a bent non-bridged MWCNT features the Yoshimura (diamond-shaped) pattern on the compressive side, where the wavelength and amplitude vary with the thickness of the MWCNT (Lourie et al., 1998; Bower et al., 1999; Poncharal et al., 1999; Liu et al., 2001; Pantano et al., 2004; Arias and Arroyo, 2008). To probe bending responses of MWCNTs, our simulation setting mimics the four-point bending experiment, where four supplementary short (10,10) SWCNTs are used, with two placed on the top, the other two on the bottom of the MWCNT under investigation. The supplementary SWCNTs are rigid and thus non-deformable. The MWCNT to be bent is 108 nm long, consisting of totally  $\sim 140,000$  degrees of freedom. The bottom two SWCNTs are 98 nm apart while the top two are 63 nm apart. By moving the top two rigid tubes downward stepwise, the central portion of the MWCNT undergoes pure bending. At each step, the entire system is relaxed and equilibrium is obtained by energy minimization. The bending moment at each step can be determined from the reaction forces and the positions of the rigid SWCNTs.

Fig. 9 shows the morphologies of the bent MWCNTs at two different applied bending curvatures,  $0.0115$  nm<sup>-1</sup> (Fig. 9(a1), (a2), and (a3)) and  $0.0137$  nm<sup>-1</sup> (Fig. 9(b1), (b2), and (b3)). In each subfigure, the three MWCNTs from top to bottom are the non-bridged,  $sp^3$ - and  $sp^2$ -bridged, respectively. The inter-wall bridge density of the bridged MWCNTs is 2%. Figs. 9 (a1) and (b1) are side views; (a2) and (b2) are longitudinal views; and (a3) and (b3) are cross-sectional views of the ridges and valleys, respectively. Our simulations show that with increasing bending curvatures, the non-bridged MWCNT transits from the uniformly deformed phase directly to the Yoshimura pattern. In contrast, the bridged MWCNTs exhibit multiple morphological phase transitions. With increasing bending curvature, the uniformly deformed phase transits to rippling pattern and finally to Yoshimura pattern, as shown in Figs. 9(a1) and (b1). The cross-sectional views of the bent MWCNTs show different configurations. For the bridged MWCNTs at the low bending curvature, the cross-sections at valleys only show little distortion from the circular shape, while those at ridges are deformed into an oval-shaped configuration. The cross-sectional views of all the bent MWCNTs with the Yoshimura pattern are similar. The cross-sections at valleys have a flattened edge; the cross-sections at ridges have two fattened edges that meet at a rounded corner. By examining the longitudinal and cross-sectional views, one notes that the innermost two shells hardly deform in the radial direction because of their relatively high radial rigidity. Rather, our simulations reveal that they are highly



**Fig. 9.** Post-buckling morphologies of bent MWCNTs. (a1) and (b1): side views; (a2) and (b2): longitudinal views; (a3) and (b3): cross-sectional views. In each subfigure, from top to bottom the MWCNTs are non-bridged,  $sp^3$ -bridged and  $sp^2$ -bridged, respectively. (a1), (a2), and (a3) are taken at  $\kappa=0.0115 \text{ nm}^{-1}$ , while (b1), (b2), and (b3) are at  $\kappa=0.0137 \text{ nm}^{-1}$ .

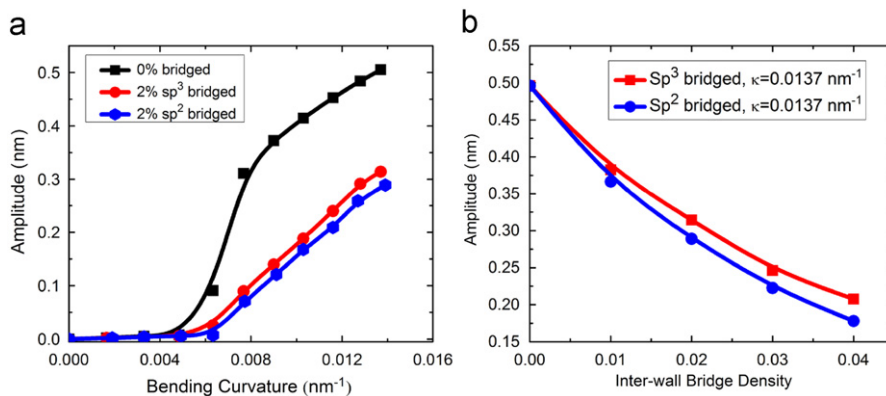


**Fig. 10.** Wave amplitude as a function of applied bending curvature (a) and of inter-wall bridge density (b).

twisted as an effective mechanism to release the elastic strain energy. Such an energy release mechanism via twisting of the inner tubes has been previously revealed by all-atom MD simulations (Li et al., 2007).

The wave amplitude as a function of the applied bending curvature and of the inter-wall bridge density is plotted in Fig. 10. Fig. 10(a) shows that the wave amplitude suddenly arises at a critical bending curvature, indicating the occurrence of buckling (rippling or Yoshimura pattern). At the same bending curvature ( $\kappa=0.0115 \text{ nm}^{-1}$ ), the wave amplitude of the non-bridged MWCNT is the largest, while that of the  $sp^2$ -bridged MWCNT is the lowest. Fig. 10(b) shows that with increasing inter-wall bridge density, the wave amplitude decreases monotonically for both  $sp^3$ - and  $sp^2$ -bridged MWCNTs. All the trends are the same as those seen in twisted MWCNTs.

Fig. 11(a) shows the bending moment vs. curvature relations. For the bridged MWCNTs, the inter-wall bridge density is 2%. The pre-buckling rigidities of the non-bridged and the  $sp^3$ -bridged MWCNTs are  $9.81 \times 10^4 \text{ nN nm}^2$ , which is fairly close to the theoretical prediction. Due to the weakening effect of the intra-wall defects, the pre-buckling rigidity of the  $sp^2$ -bridged MWCNT is  $9.38 \times 10^4 \text{ nN nm}^2$ , slightly lower than the other two MWCNTs. It should be mentioned that the inter-wall bridges have little effect on the pre-buckling rigidity because they remain intact in this loading regime. Compared to the non-bridged MWCNT, the bridged MWCNTs have much higher post-buckling rigidities. In addition, the rippling and buckling regimes have the similar rigidities. The post-buckling rigidities of the bridged MWCNTs are comparable to the pre-buckling rigidity, demonstrating that the bridges play a strong strengthening role. Fig. 11(b) plots the post-buckling rigidities of the bridged MWCNTs normalized by that of the non-bridged MWCNT as a function of the inter-wall bridge density. For the  $sp^3$ -bridged MWCNT, its post-buckling rigidity increases nearly linearly with the inter-wall bridge density. It is expected that at the saturated inter-wall bridge density, the bridged MWCNT resembles amorphous diamond structures, and its rigidity should be close to that of a nano-diamond. While for the  $sp^2$ -bridged

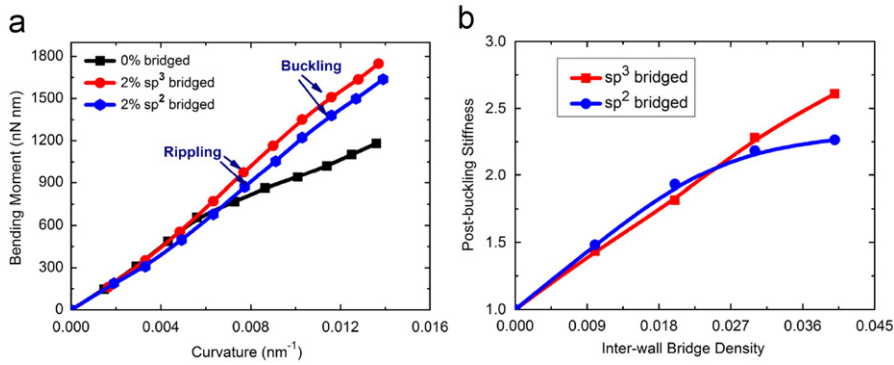


Fig. 11. (a) Bending response of a 10-layer MWCNT and (b) post-buckling rigidity as a function of inter-wall bridge density.

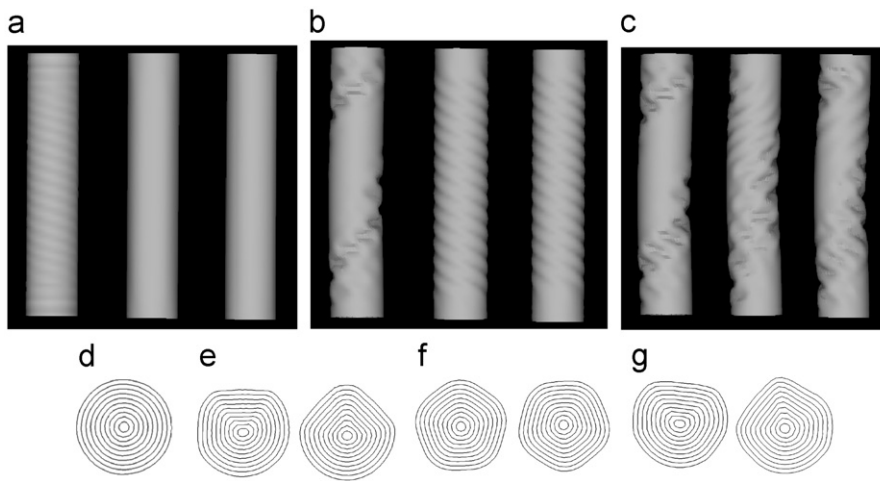


Fig. 12. Deformation morphologies of uniaxially compressed MWCNTs. (a)–(c) Longitudinal views of the three MWCNTs. In each subfigure from left to right, the MWCNTs are non-bridged, 4% sp<sup>3</sup>-bridged, and 4% sp<sup>2</sup>-bridged. The compressive strains are 0.015 in (a), 0.032 in (b), and 0.04 in (c). (d)–(g) Cross-sectional views of the left MWCNTs in (a), of ridges and valleys of the left and central MWCNTs in (b), and of the central MWCNT in (c), respectively.

MWCNT, because of the weakening effects of the defects involved, the post-buckling rigidity increases nonlinearly and approaches its maximum at  $\rho=4\%$ .

### 3.3. Compression

Our previous studies showed that under uniaxial compression the constituent shells in MWCNTs buckle in a coordinated manner (Huang et al., 2010). Due to the large discrepancy of the aspect ratios of the inner and outer shells, the outer shell undergoes shell buckling, while the inner shell undergoes beam buckling. The coordinated buckling mechanism results in helical diamond pattern on the outer shells, while the innermost shell undergoes internal twisting and bending, featuring a spiral configuration. Though each graphene shell behaves nonlinearly, the mechanical response of thick MWCNTs under uniaxial compression follows a bilinear law, where the ratio of the post-buckling rigidity to the pre-buckling rigidity is a constant, independent of the tube diameter.

Fig. 12 shows the post-buckling morphologies of the compressed MWCNTs at three different applied compressive strains  $\epsilon$ , 0.015 (a), 0.032 (b), and 0.04 (c). In each subfigure, the three configurations from left to right are for the non-bridged, 4% sp<sup>3</sup>-bridged and 4% sp<sup>2</sup>-bridged MWCNTs. At the compressive strain of 0.015, only the non-bridged MWCNT ripples. At the moderate compressive strain of 0.032, the bridged MWCNTs ripple, while the non-bridged MWCNT exhibits a helically arranged diamond pattern. At a still larger compressive strain, the amplitude of the rippling pattern in the non-bridged MWCNT increases, while the rippling and diamond patterns coexist in the bridged MWCNTs. Fig. 12(d) shows the cross-sectional view of the left-most tube in (a), where the radial distortion due to rippling is hardly distinguishable. Fig. 12(e) shows cross-sections at ridges (left) and valleys (right) of the left-most tube in Fig. 12(b). A flattened edge appears in the cross-sections at the ridges, while a sharp corner appears in the cross-sections at valleys. These cross-sectional views shown in Fig. 12(f) correspond to the central tube in Fig. 12(b), where the cross-sections at ridges (left) and

valleys (right) are in polygonal shape. The cross-sectional views at a higher compressive strain, as shown in Fig. 12(g), are similar to (e), except that the cross-sections are even further distorted.

Fig. 13 shows the stress–strain curves for the 4%  $sp^3$ - and  $sp^2$ - and non-bridged MWCNTs. For the non-bridged MWCNT, the reaction force abruptly drops at the buckling strain. While for bridged MWCNT, the reaction force does not drop appreciably when rippling occurs. The reaction force continues to increase nearly linearly in the rippling regime. The decreasing of the reaction force is observed after the MWCNT reaches its secondary instability (buckling) strain at which helically arranged diamond pattern appears. We note that the harmonic and post-rippling rigidities are nearly the same, and the entire mechanical responses of the MWCNT prior to Yoshimura pattern can be characterized by a simple linear law. Compared to the non-bridged MWCNT, the linear regime of 4% bridged MWCNT has been strengthened by  $\sim 180\%$ . In the Yoshimura regime, however, the post-buckling rigidities are negative, which appears to agree with previous experimental data (Yap et al., 2007). Fig. 13(b) shows the post-buckling rigidities of the bridged MWCNTs normalized by that of the non-bridged MWCNT as a function of the inter-wall bridge density. Similar to the trend observed for the post-buckling rigidity of the bent MWCNTs, the post-buckling rigidity of the  $sp^3$ -bridged MWCNT increases with increasing inter-wall bridge density. While for the  $sp^2$ -bridged MWCNTs, the post-rippling rigidity reaches a maximum at  $\rho \sim 0.3$ . For both  $sp^3$ - and  $sp^2$ -bridged MWCNTs, the post-rippling rigidities are much larger (6–8 times) than that of non-bridged MWCNTs.

#### 4. Energetics of evolving deformation morphologies

The load-driven multiple morphological phase stability calls for detailed analyses. In Fig. 14(a) and (b), we constructed deformation phase diagrams for both  $sp^3$ - and  $sp^2$ -bridged MWCNTs under bending in the plane of bending curvature  $\kappa$  (unit:  $\text{nm}^{-1}$ ) and inter-wall bridge density  $\rho$ . At a fixed bridge density, for low bending curvatures, the MWCNTs behave as elastic beams and are uniformly bent (phase I). When the bending curvature increases and reaches a critical value, wave-like periodic rippling pattern (phase II) appears. Such rippling pattern resembles that observed in twisted MWCNTs (Huang et al., 2008b). With further increased bending curvature, the rippling pattern transits into the Yoshimura pattern

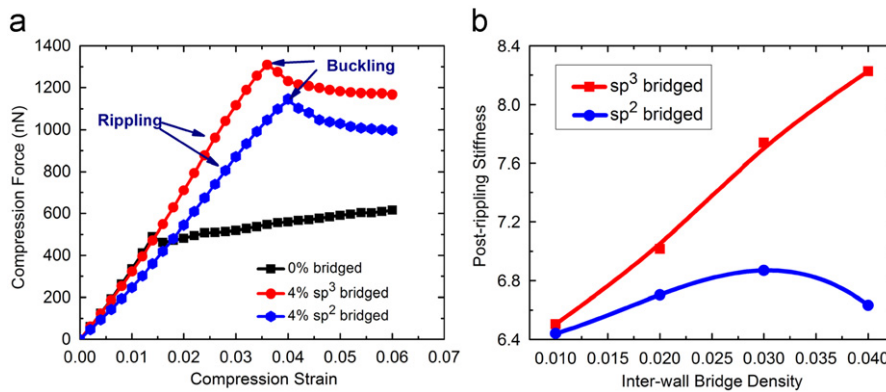


**Fig. 13.** (a) Stress–strain relation for the uniaxially compressed MWCNTs. For the bridged MWCNT, rippling occurs at much larger compressive strains. The post-rippling rigidities of the bridged MWCNTs are much larger than the post-buckling rigidity of the non-bridged MWCNT. The post-buckling rigidities of the MWCNTs, however, are negative. Rippling and buckling points are indicated. (b) With increasing inter-wall bridge density, the post-rippling rigidity increases for  $sp^3$ -bridged MWCNTs. While for the  $sp^2$ -bridged MWCNTs, the post-rippling rigidity reaches a maximum at  $\rho \sim 0.3$ .

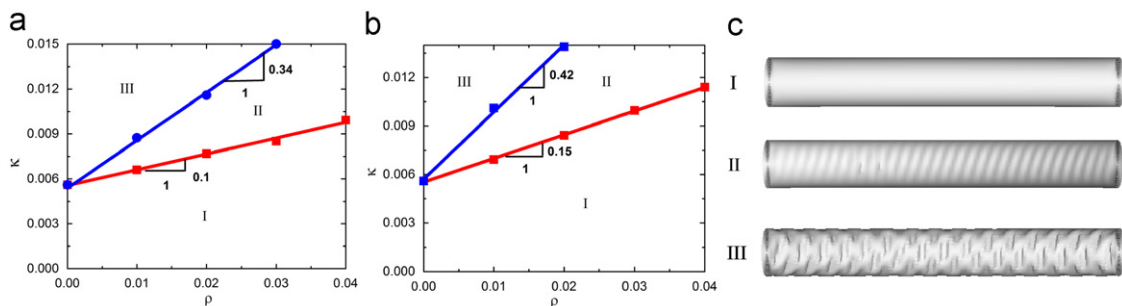


**Fig. 14.** The phase diagram of deformation morphologies of the bridged MWCNTs on the plane of bending curvature and interlayer bonding density. (a) The phase diagram for  $sp^3$ -bridged MWCNTs. (b) The phase diagram for  $sp^2$ -bridged MWCNTs. (c) Three deformation phases: (I) uniformly deformed phase; (II) rippling phase; and (III) Yoshimura phase.

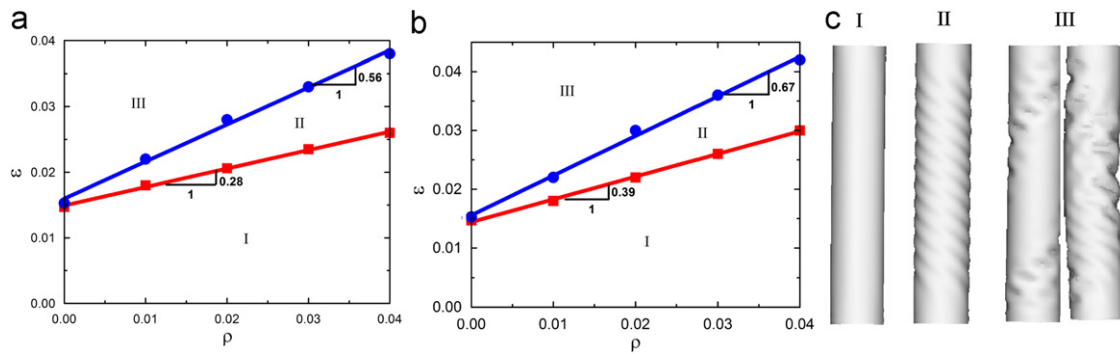


**Fig. 15.** The phase diagram of deformation morphologies of the uniaxially compressed MWCNTs in the plane of compressive strain and inter-wall bridge density. (a) The phase diagram for  $sp^3$ -bridged MWCNTs. (b) The phase diagram for  $sp^2$ -bridged MWCNTs. (c) Three deformation phases: (I) uniformly deformed phase; (II) rippling phase; and (III) helically arranged diamond pattern or coexisting phase.

(phase III). The longitudinal views of the three characteristic morphologies on the bent side of the MWCNT are shown on the right of Fig. 14. The rippling pattern is absent in the non-bridged MWCNT ( $\rho=0$ ); the uniformly deformed phase transits directly into the Yoshimura pattern at the critical curvature of  $0.0056 \text{ nm}^{-1}$ . Increasing the inter-wall bridge density effectively widens the curvature range within which rippling pattern appears. For both bridge types, the transition curvatures linearly scale with the inter-wall bridging density, giving rise to linear phase boundaries. The slopes of these linear phase boundaries are indicated in the figure. The linear scaling manifests the strengthening effect of the interlayer bridges against structural instability.

Fig. 15 shows the phase diagrams of the bridged MWCNTs under uniaxial compression, where the regimes of the uniformly deformed (I), rippled (II), and diamond or coexisting (III) phases are indicated in the space of the compressive strain  $\epsilon$  and the inter-wall bridge density  $\rho$ . The phase transition boundaries are all nearly linear, and the slopes of the transition boundaries are indicated in Fig. 15(a) and (b) for the  $sp^3$ -bridged and  $sp^2$ -bridged MWCNTs, respectively. The rippling pattern hardly occurs for the non-bridged MWCNT ( $\rho=0$ ); the uniformly deformed phase transits almost directly into the Yoshimura pattern at the critical compressive strain of 0.015. Due to the presence of the inter-wall covalent bridges, the coordinated nature of the buckling of the constituent shells is pronounced. For the non-bridged MWCNT, the instability strains for the rippling and diamond patterns are very close to each other. With increasing inter-wall bridge density, the instability strains for these two patterns increase linearly, similar to the linear phase boundaries in bent MWCNTs. Overall, the regime for rippling pattern is rather narrow. It should be noted that at large compressive strains, the rippling and diamond patterns coexist for bridged MWCNTs. While for non-bridged MWCNT, only helically arranged diamond pattern appears.

Using the bent  $sp^3$ -bridged MWCNT as an example, we next elucidate the deformation energetics that governs the morphological phase transition. We decompose the total strain energy into the in-plane deformation energy and inter-wall interaction energy. From our simulation results we identify the two phase transition points that separate the three deformation phases. The energy curves for these three phases are, respectively, plotted by black, blue, and red symbols connected by solid lines, as shown in Fig. 16(a) and (b) ( $\rho=2\%$ ). To rationalize why rippling pattern appears at moderate bending curvatures, we compare the relative energetics of the rippling pattern and the Yoshimura pattern (as if it would occur) in the rippling regime. We extrapolate the curve segments in the Yoshimura regime backward to the rippling regime (solid red lines in Fig. 16(a) and (b)). We then shift the extrapolated segment such that the extrapolated segment starts from the transition point from the uniformly deformed phase to the rippling phase. The shifted segments, marked by dashed red lines in Fig. 16(a) and (b), correspond to the case as if the Yoshimura pattern would occur beyond the uniformly deformed phase. We found that the dashed red segment is below the blue segment in Fig. 16(a), but above in Fig. 16(b). This comparison suggests that if replacing the rippling pattern by the Yoshimura pattern at moderate curvatures, it would cause less in-plane strain energy, but larger inter-wall energy penalty. The differences of the in-plane and inter-wall interaction energies are plotted in the insets of Fig. 16(a) and (b), respectively. The total energy difference ( $\Delta E_{\text{Total}} = E_{\text{Yoshimura}} - E_{\text{Rippling}}$ ) is plotted in Fig. 16(c) and (d), which gives rise to the relative stability of the rippling pattern and the Yoshimura pattern. In the rippling regime, the energy difference vanishes at the two phase transition points, and is always positive in between. This energetics analysis indicates that in the rippling regime the inter-wall bridging energy dominates the physics. In this regime, the Yoshimura pattern involves very high inter-wall energy penalty, and is thus energetically disfavored. We also extrapolate the energy curves of the rippling regime forward to the Yoshimura regime and compare accordingly the energetics. The total energy difference monotonically decreases in the Yoshimura regime, as plotted in Fig. 16(d). In this regime, the in-plane deformation energy dominates the physics. The rippling pattern involves much higher in-plane deformation energy than the Yoshimura pattern in this regime, and is thus energetically disfavored. We have also performed similar energetics analysis for the case of uniaxial compression and reached the similar conclusions.

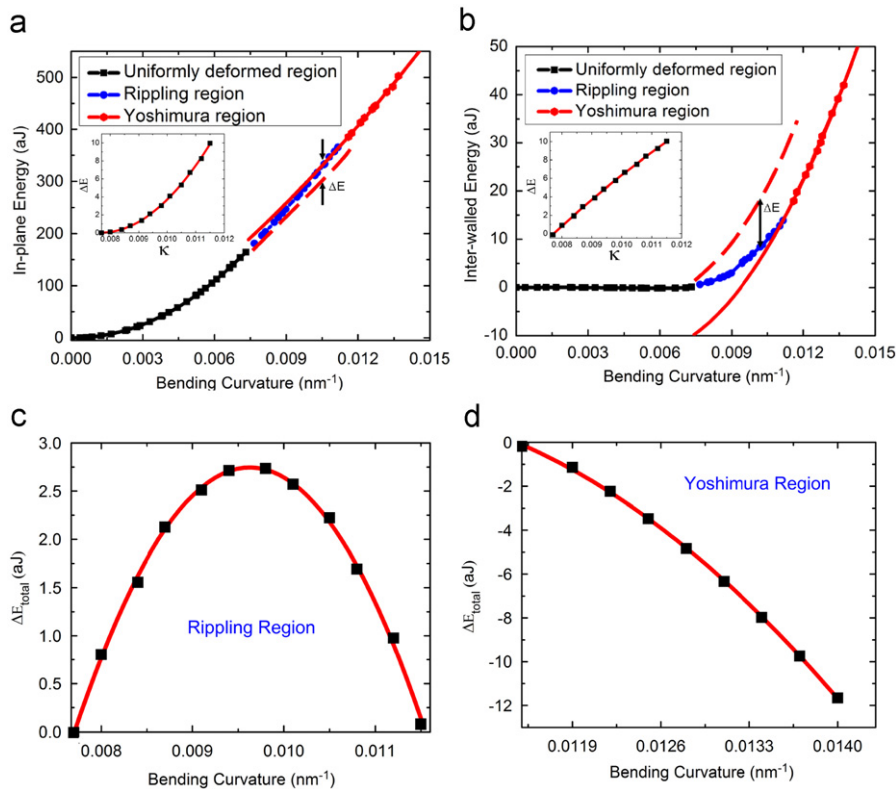


**Fig. 16.** Energetics analysis of morphological phase transitions in the 10-walled MWCNT under pure bending. (a) In-plane strain energy and (b) inter-wall interaction energy. In (a) and (b), the energy curves for the uniformly deformed phase, the rippling phase, and the Yoshimura phase are, respectively, plotted by black, blue and red symbols connected by solid lines. The extrapolated segments from the energy curve of the Yoshimura phase downward to the rippling phases are shifted and plotted by dashed red lines. The insets plot the energy difference of the rippling pattern and the Yoshimura pattern in the rippling regime. (c) The total energy difference of the rippling and Yoshimura patterns in the rippling regime. (d) The total energy difference of the rippling and Yoshimura patterns in the Yoshimura regime. (For interpretation of the references to color in this figure legend, the reader is referred to the web version of this article.)

## 5. Discussions and conclusions

We analyzed the deformation morphologies and energetics of covalently bridged MWCNTs within a multiscale modeling framework. Since the constitutive model of the interatomic potential based hyperelasticity incorporates the nonlinearity of the intra-wall graphene shell deformation and the cohesive energies originated from the inter-wall vdW interactions and covalent bridges, the multiscale model is well suited to the study of nonlinear deformation of MWCNTs while maintaining fidelity with the underlying atomistic responses. The efficiency of numerical framework permits the simulation of significantly larger systems than atomistically accessible. However, the quasi-continuum model is only valid when spatial variation of the continuum deformation field is gradual on the atomic scale, and thus cannot address defect motions that involve strain localization and deformation discontinuity (Li et al., 2004; Dumitrica et al., 2006; Zhang and Zhu, 2007; Huang et al., 2008a, 2009; Terdalkar et al., 2010). Applicability of the simulation model is also limited to low inter-wall bridge density. At a high bridge density, the interstitials associated with  $sp^3$  bridges would interact to form extra covalent bonds; the vacancy defects associated with the  $sp^2$  bridges would be sufficiently close to each other and hence interact to form large open ring structures from which fracture initiates. Special care needs to be taken to include such chemical processes that are out of the scope of the present study.

The deformation morphologies of MWCNTs have motivated continual research because of the fundamentally different deformation mechanisms compared to that of SWCNT buckling. Our simulation results show that the presence of inter-wall bridges significantly enhances the post-buckling rigidities. While the strengthening effect of inter-wall bridges is expected, their role in modifying the deformation morphology pathways is rather intriguing. For both bending and uniaxial compression, the bridged MWCNTs ripple as the first buckling mechanism; further increasing the applied load drives the morphology into the Yoshimura regime. This is in distinct contrast to the morphological transition from uniform deformation directly to Yoshimura pattern in non-bridged MWCNTs predicted by many previous studies (Arroyo and Belytschko, 2003; Pantano et al., 2003; Li et al., 2007; Arias and Arroyo, 2008; Arroyo and Arias, 2008). Within the rippling regime, the rigidities of the bridged MWCNT do not suffer drastic loss. The rippling regime is amplified with increasing

inter-wall bridge density. This result suggests that tailoring the inter-wall interaction energies thus can modulate the deformation morphologies (Xu et al., 2008). Indeed, confirmed by our simulations, non-bridged MWCNTs with an inter-wall distance smaller than 0.34 nm would favor rippling pattern and follow the evolving deformation pathways of the bridged MWCNTs studied here. Owing to the elastic nature of the deformation, the morphological phase transitions are reversible upon unloading, which suggests that such MWCNTs may be designed as shape-memory devices with tunable stabilities. The multiple phase transitions in deformed MWCNTs not only influence the mechanical properties of the MWCNTs, but also alter their electronic properties. Our study therefore opens new pathways of tuning the electronic properties of MWCNTs through mechanical loading.

## Acknowledgement

We gratefully acknowledge the grants support from the National Science Foundation grant under award no. 0600661 and 1042319.

## Reference

- Arias, I., Arroyo, M., 2008. Size-dependent nonlinear elastic scaling of multiwalled carbon nanotubes. *Phys. Rev. Lett.* 100 (8), 085503.
- Arroyo, M., Arias, I., 2008. Rippling and a phase-transforming mesoscopic model for multiwalled carbon nanotubes. *J. Mech. Phys. Solids* 56 (4), 1224–1244.
- Arroyo, M., Belytschko, T., 2002. An atomistic-based finite deformation membrane for single layer crystalline films. *J. Mech. Phys. Solids* 50 (9), 1941–1977.
- Arroyo, M., Belytschko, T., 2003. Nonlinear mechanical response and rippling of thick multiwalled carbon nanotubes. *Phys. Rev. Lett.* 91 (21), 215505.
- Arroyo, M., Belytschko, T., 2004. Finite crystal elasticity of carbon nanotubes based on the exponential Cauchy–Born rule. *Phys. Rev. B* 69 (11), 115415.
- Belytschko, T., Xiao, S.P., Schatz, G.C., Ruoff, R.S., 2002. Atomistic simulations of nanotube fracture. *Phys. Rev. B* 65 (23), 235430.
- Bower, C., Rosen, R., Jin, L., Han, J., Zhou, O., 1999. Deformation of carbon nanotubes in nanotube-polymer composites. *Appl. Phys. Lett.* 74 (22), 3317–3319.
- Brenner, D.W., Shenderova, O.A., Harrison, J.A., Stuart, S.J., Ni, B., Sinnott, S.B., 2002. A second-generation reactive empirical bond order (REBO) potential energy expression for hydrocarbons. *J. Phys.: Condens. Mat.* 14 (4), 783–802.
- Buehler, M.J., 2006. Mesoscale modeling of mechanics of carbon nanotubes: self-assembly, self-folding, and fracture. *J. Mater. Res.* 21 (11), 2855–2869.
- Cao, G.X., Chen, X., 2006. Buckling of single-walled carbon nanotubes upon bending: molecular dynamics simulations and finite element method. *Phys. Rev. B* 73 (15), 155435.
- Chang, T.C., Gao, H.J., 2003. Size-dependent elastic properties of a single-walled carbon nanotube via a molecular mechanics model. *J. Mech. Phys. Solids* 51 (6), 1059–1074.
- Dumitrica, T., Hua, M., Yakobson, B.I., 2006. Symmetry-, time-, and temperature-dependent strength of carbon nanotubes. *Proc. Natl. Acad. Sci. USA* 103 (16), 6105–6109.
- Falvo, M.R., Clary, G.J., Taylor, R.M., Chi, V., Brooks, F.P., Washburn, S., Superfine, R., 1997. Bending and buckling of carbon nanotubes under large strain. *Nature* 389 (6651), 582–584.
- Fennimore, A.M., Yuzvinsky, T.D., Han, W.Q., Fuhrer, M.S., Cumings, J., Zettl, A., 2003. Rotational actuators based on carbon nanotubes. *Nature* 424 (6947), 408–410.
- Gao, H.J., Kong, Y., Cui, D.X., Ozkan, C.S., 2003. Spontaneous insertion of DNA oligonucleotides into carbon nanotubes. *Nano Lett.* 3 (4), 471–473.
- Girifalco, L.A., Hodak, M., Lee, R.S., 2000. Carbon nanotubes, buckyballs, ropes, and a universal graphitic potential. *Phys. Rev. B* 62 (19), 13104–13110.
- Huang, J.Y., Ding, F., Yakobson, B.I., 2008a. Dislocation dynamics in multiwalled carbon nanotubes at high temperatures. *Phys. Rev. Lett.* 100 (3), 035503.
- Huang, J.Y., Ding, F., Yakobson, B.I., Lu, P., Qi, L., Li, J., 2009. In situ observation of graphene sublimation and multi-layer edge reconstructions. *Proc. Natl. Acad. Sci. USA* 106 (25), 10103–10108.
- Huang, X., Yuan, H.Y., Hsia, K.J., Zhang, S.L., 2010. Coordinated buckling of thick multi-walled carbon nanotubes under uniaxial compression. *Nano Res.* 3 (1), 32–42.
- Huang, X., Zou, J., Zhang, S.L., 2008b. Bilinear responses and rippling morphologies of multiwalled carbon nanotubes under torsion. *Appl. Phys. Lett.* 93 (3), 031915.
- Iijima, S., Brabec, C., Maiti, A., Bernholc, J., 1995. Structural flexibility of carbon nanotubes. *J. Chem. Phys.* 104 (5), 2089–2092.
- Khare, R., Mielke, S.L., Paci, J.T., Zhang, S.L., Ballarini, R., Schatz, G.C., Belytschko, T., 2007. Coupled quantum mechanical/molecular mechanical modeling of the fracture of defective carbon nanotubes and graphene sheets. *Phys. Rev. B* 75 (7), 075412.
- Kis, A., Csanyi, G., Salvétat, J.P., Lee, T.N., Couteau, E., Kulik, A.J., Benoit, W., Brugger, J., Forro, L., 2004. Reinforcement of single-walled carbon nanotube bundles by intertube bridging. *Nat. Mater.* 3 (3), 153–157.
- Kolmogorov, A.N., Crespi, V.H., 2000. Smoothest bearings: interlayer sliding in multiwalled carbon nanotubes. *Phys. Rev. Lett.* 85 (22), 4727–4730.
- Krasheninnikov, A.V., Lehtinen, P.O., Foster, A.S., Nieminen, R.M., 2006. Bending the rules: contrasting vacancy energetics and migration in graphite and carbon nanotubes. *Chem. Phys. Lett.* 418 (1–3), 132–136.
- Krasheninnikov, A.V., Nordlund, K., Keinonen, J., 2002. Production of defects in supported carbon nanotubes under ion irradiation. *Phys. Rev. B* 65 (16), 165423.
- Lee, C., Wei, X.D., Kysar, J.W., Hone, J., 2008. Measurement of the elastic properties and intrinsic strength of monolayer graphene. *Science* 321 (5887), 385–388.
- Legoas, S.B., Coluci, V.R., Braga, S.F., Coura, P.Z., Dantas, S.O., Galvao, D.S., 2003. Molecular-dynamics simulations of carbon nanotubes as gigahertz oscillators. *Phys. Rev. Lett.* 90 (5), 055504.
- Li, J., Zhu, T., Yip, S., Van Vliet, K.J., Suresh, S., 2004. Elastic criterion for dislocation nucleation. *Mat. Sci. Eng. A—Struct.* 365 (1–2), 25–30.
- Li, X.Y., Yang, W., Liu, B., 2007. Bending induced rippling and twisting of multiwalled carbon nanotubes. *Phys. Rev. Lett.* 98 (20), 205502.
- Liu, D.C., Nocedal, J., 1989. On the limited memory bfgs method for large-scale optimization. *Math. Program.* 45 (3), 503–528.
- Liu, J.Z., Zheng, Q.S., Jiang, Q., 2001. Effect of a rippling mode on resonances of carbon nanotubes. *Phys. Rev. Lett.* 86 (21), 4843–4846.
- Liu, J.Z., Zheng, Q.S., Jiang, Q., 2003. Effect of bending instabilities on the measurements of mechanical properties of multiwalled carbon nanotubes. *Phys. Rev. B* 67 (7), 075414.
- Lourie, O., Cox, D.M., Wagner, H.D., 1998. Buckling and collapse of embedded carbon nanotubes. *Phys. Rev. Lett.* 81 (8), 1638–1641.
- Mielke, S.L., Troya, D., Zhang, S., Li, J.L., Xiao, S.P., Car, R., Ruoff, R.S., Schatz, G.C., Belytschko, T., 2004. The role of vacancy defects and holes in the fracture of carbon nanotubes. *Chem. Phys. Lett.* 390 (4–6), 413–420.
- Mielke, S.L., Zhang, S., Khare, R., Ruoff, R.S., Belytschko, T., Schatz, G.C., 2007. The effects of extensive pitting on the mechanical properties of carbon nanotubes. *Chem. Phys. Lett.* 446 (1–3), 128–132.

- Milstein, F., 1982. In: *Mechanics of Solids*. Pergamon, Oxford.
- Pantano, A., Boyce, M.C., Parks, D.M., 2003. Nonlinear structural mechanics based modeling of carbon nanotube deformation. *Phys. Rev. Lett.* 91 (14), 145504.
- Pantano, A., Parks, D.M., Boyce, M.C., 2004. Mechanics of deformation of single- and multi-wall carbon nanotubes. *J. Mech. Phys. Solids* 52 (4), 789–821.
- Poncharal, P., Wang, Z.L., Ugarte, D., 1999. Electrostatic deflections and electromechanical resonances of carbon nanotubes. *Science* 283 (5407), 1513–1516.
- Qian, D., Dickey, E., Andrews, R., Rantell, T., 2000. Load transfer and deformation mechanisms in carbon nanotube–polystyrene composites. *Appl. Phys. Lett.* 76 (20), 2868–2870.
- Shenderova, O.A., Brenner, D.W., Omeltchenko, A., Su, X., Yang, L.H., 2000. Atomistic modeling of the fracture of polycrystalline diamond. *Phys. Rev. B* 61 (6), 3877–3888.
- Shenoy, V.B., Reddy, C.D., Ramasubramaniam, A., Zhang, Y.W., 2008. Edge-stress-induced warping of graphene sheets and nanoribbons. *Phys. Rev. Lett.* 101 (24), 245501.
- Song, H.Y., Zha, X.W., 2009. Molecular dynamics study of effects of  $sp^3$  interwall bridging upon torsional behavior of double-walled carbon nanotube. *Phys. Lett. A* 373 (6), 682–685.
- Telling, R.H., Ewels, C.P., El-Barbary, A.A., Heggge, M.I., 2003. Wigner defects bridge the graphite gap. *Nat. Mater.* 2 (5), 333–337.
- Terdalkar, S.S., Huang, S., Yuan, H.Y., Rencis, J.J., Zhu, T., Zhang, S.L., 2010. Nanoscale fracture in graphene. *Chem. Phys. Lett.* 494 (4–6), 218–222.
- Terdalkar, S.S., Zhang, S.L., Rencis, J.J., Hsia, K.J., 2008. Molecular dynamics simulations of ion-irradiation induced deflection of 2D graphene films 45 (13), 3908–3917. *Int. J. Solids Struct.* 45 (13), 3908–3917.
- Tomblor, T., Zhou, C., Alexseyev, L., 2000. Reversible electromechanical characteristics of carbon nanotubes under local-probe manipulation. *Nature* 405, 769–772.
- Xia, Z.H., Guduru, P.R., Curtin, W.A., 2007. Enhancing mechanical properties of multiwall carbon nanotubes via  $sp^3$  interwall bridging. *Phys. Rev. Lett.* 98 (24), 245501.
- Xu, Z.P., Wang, L.F., Zheng, Q.S., 2008. Enhanced mechanical properties of prestressed multi-walled carbon nanotubes. *Small* 4 (6), 733–737.
- Yakobson, B.I., Brabec, C.J., Bernholc, J., 1996. Nanomechanics of carbon tubes: Instabilities beyond linear response. *Phys. Rev. Lett.* 76 (14), 2511–2514.
- Yang, L., Han, J., 2000. Electronic structure of deformed carbon nanotubes. *Phys. Rev. Lett.* 85 (1), 154–157.
- Yap, H.W., Lakes, R.S., Carpick, R.W., 2007. Mechanical instabilities of individual multiwalled carbon nanotubes under cyclic axial compression. *Nano Lett.* 7 (5), 1149–1154.
- Zhang, P., Huang, Y., Geubelle, P.H., Klein, P.A., Hwang, K.C., 2002. The elastic modulus of single-wall carbon nanotubes: a continuum analysis incorporating interatomic potentials. *Int. J. Solids Struct.* 39 (13–14), 3893–3906.
- Zhang, S., Zhu, T., 2007. Atomic geometry and energetics of carbon nanotube necking. *Philos. Mag. Lett.* 87 (8), 567–574.
- Zhang, S.L., Khare, R., Lu, Q., Belytschko, T., 2007a. A bridging domain and strain computation method for coupled atomistic-continuum modelling of solids. *Int. J. Numer. Meth. Eng.* 70 (8), 913–933.
- Zhang, S.L., Liu, W.K., Ruoff, R.S., 2004a. Atomistic simulations of double-walled carbon nanotubes (DWCNTs) as rotational bearings. *Nano Lett.* 4 (2), 293–297.
- Zhang, S.L., Mielke, S.L., Khare, R., Troya, D., Ruoff, R.S., Schatz, G.C., Belytschko, T., 2005. Mechanics of defects in carbon nanotubes: atomistic and multiscale simulations. *Phys. Rev. B* 71 (11), 115403.
- Zhang, S.L., Wagner, G., Medyanik, S.N., Liu, W.K., Yu, Y.H., Chung, Y.W., 2004b. Experimental and molecular dynamics simulation studies of friction behavior of hydrogenated carbon films. *Surf. Coat. Tech.* 177, 818–823.
- Zhang, S.L., Zhu, T., Belytschko, T., 2007b. Atomistic and multiscale analyses of brittle fracture in crystal lattices. *Phys. Rev. B* 76 (9), 094114.
- Zheng, Q.S., Jiang, Q., 2002. Multiwalled carbon nanotubes as gigahertz oscillators. *Phys. Rev. Lett.* 88, 45503.
- Zou, J., Huang, X., Arroyo, M., Zhang, S.L., 2009. Effective coarse-grained simulations of super-thick multi-walled carbon nanotubes under torsion. *J. Appl. Phys.* 105, 033516.
- Zou, J., Ji, B.H., Feng, X.Q., Gao, H.J., 2006. Self-assembly of single-walled carbon nanotubes into multiwalled carbon nanotubes in water: molecular dynamics simulations. *Nano Lett.* 6 (3), 430–434.
- Zou, J., Liang, W.T., Zhang, S.L., Coarse-grained molecular dynamics modeling of DNA–carbon nanotube complexes. *Int. J. Numer. Meth. Eng.*, in press, doi:10.1002/nme.2819.